APL Materials

The nature of column boundaries in micro-structured silicon oxide nanolayers

Cite as: APL Mater. 9, 121107 (2021); https://doi.org/10.1063/5.0073349
Submitted: 29 September 2021 • Accepted: 27 November 2021 • Published Online: 08 December 2021

K. Patel, J. Cottom, A. Mehonic, et al.

The nature of column boundaries in micro-structured silicon oxide nanolayers

Cite as: APL Mater. 9, 121107 (2021); doi: 10.1063/5.0073349
Submitted: 29 September 2021 • Accepted: 27 November 2021 •
Published Online: 8 December 2021

K. Patel,[1,2] J. Cottom,[1] A. Mehonic,[3,a)] W. H. Ng,[3] A. J. Kenyon,[3] M. Bosman,[2,4] and A. L. Shluger[1]

AFFILIATIONS

[1] Department of Physics and Astronomy, University College London, Gower Street, London WC1E 6BT, United Kingdom
[2] Institute of Materials Research and Engineering, A*STAR (Agency for Science, Technology and Research), 2 Fusionopolis Way, Singapore 138634, Singapore
[3] Department of Electronic and Electrical Engineering, University College London, Gower Street, London WC1E 6BT, United Kingdom
[4] Department of Materials Science and Engineering, National University of Singapore, 9 Engineering Drive 1, Singapore 117575, Singapore

Note: This paper is part of the Special Topic on Materials Challenges for Nonvolatile Memory.
[a)] **Author to whom correspondence should be addressed:** adnan.mehonic.09@ucl.ac.uk

ABSTRACT

Columnar microstructures are critical for obtaining good resistance switching properties in SiO_x resistive random access memory (ReRAM) devices. In this work, the formation and structure of columnar boundaries are studied in sputtered SiO_x layers. Using TEM measurements, we analyze SiO_x layers in Me–SiO_x–Mo heterostructures, where Me = Ti or Au/Ti. We show that the SiO_x layers are templated by the Mo surface roughness, leading to the formation of columnar boundaries protruding from troughs at the SiO_x/Mo interface. Electron energy-loss spectroscopy measurements show that these boundaries are best characterized as voids, which in turn facilitate Ti, Mo, and Au incorporation from the electrodes into SiO_x. Density functional theory calculations of a simple model of the SiO_2 grain boundary and column boundary show that O interstitials preferentially reside at the boundaries rather than in the SiO_2 bulk. The results elucidate the nature of the SiO_x microstructure and the complex interactions between the metal electrodes and the switching oxide, each of which is critically important for further materials engineering and the optimization of ReRAM devices.

I. INTRODUCTION

Over the last 20 years, various resistive random access memory (ReRAM) devices have been studied to produce the next generation of nonvolatile memory technology, currently dominated by flash memory. ReRAM offers a range of advantages over the incumbent memory technologies in terms of programming speed, higher endurance, and potentially better energy efficiency.[1–3] However, mass adoption has been slow due to high device variability and difficulties associated with CMOS integration and materials compatibility.[4] Beyond digital memory, ReRAM technology is also considered for deep learning accelerators and neuromorphic systems.[5,6] The devices are typically based on oxides, with interest being focused on a variety of transition metal, rare earth, and main group oxides, with varying degrees of success. Regardless of the choice of dielectric, ReRAM devices operate by the field-induced switching between a high resistance state (HRS) and at least one low resistance state (LRS). Filamentary ReRAM devices are driven by the formation and modulation of conductive filaments (CFs) by appropriate external electric fields.[7,8] The most critical measures of device performance include the forming and switching voltages, programming speed, high endurance, good retention, and low variability of both resistance states and switching voltages.

A variety of oxides have been tested, with great promise being shown by devices based on HfO_2, TaO_x, and other binary oxides.[9] Recently, interest has turned to SiO_2 and the related suboxide (SiO_x), as they offer a variety of benefits from the processing, cost, and fabrication perspectives.[10,11] The processing and handling benefits are derived from the abundance of SiO_2 expertise in CMOS technology, particularly in the growth and characterization of SiO_2

films. Intrinsic resistance switching in SiO_x has been less studied due to the historical perception that SiO_2 is not easily reducible and, thus, thin layers are passive insulators not suited to ReRAM devices with high performance. Furthermore, it has been claimed explicitly that resistance switching in undoped SiO_x is impossible.[12] However, more recently, it has been shown that more deliberate engineering of microstructures in SiO_x layers produces ReRAM devices with excellent switching properties.[11,13] SiO_x-based devices can be divided into two main types: extrinsic, those based on the inter-diffusion of metal ions, such as via electrochemical metallization or doping, and intrinsic, those where a CF is formed as a result of reduction under bias application, so called valence change memory (VCM).[7,14] Some of the most promising VCM devices comprise metal/SiO_x/metal stacks produced by sputter deposition of the SiO_x and electrodes. Sputter deposition imparts significant complexity to the structure of the layers beyond the already amorphous oxide and polycrystalline electrodes. Initial work by Munde *et al.*[15] has shown significant redistribution of O on cycling, with Mehonic *et al.*[13] measuring the release of O. These studies have demonstrated the presence of a columnar microstructure within the oxide, but the resolution was insufficient to determine the character of columnar structures and boundaries.[15] It was postulated that these could be voids, low density regions, and/or a result of the redistribution of O on forming. Although it is clear that the presence of structural columns promotes the formation of conductive filaments and decreases the electroforming voltages,[13,15] the structure and chemical composition of columns remain a mystery.

Since the prospect of SiO_x ReRAM devices is highly appealing due to their CMOS compatibility and easier integration, it is critical to better understand the nature of columns and column boundaries (CBs) in amorphous SiO_x devices to realize their full potential. Developing further understanding of the film microstructure should allow us to refine the models of device operation and subsequently use this understanding to optimize the next generation of devices. In a wider sense, deeper understanding of the structure and chemical composition of columns is important not only for SiO_x structures but also for a much broader range of oxide films, such as CeO_x[16] and SnO_2[17] used as anodes in solid oxide fuel cells, TiO_2 used in optical devices,[18] $SrTiO_3$ and $BaTiO_3$,[19] and many others. Although they are grown using very different deposition methods, they share the columnar morphology.

Further understanding of the electronic properties of these complex disordered interfaces can be assisted by theoretical simulations. However, progress in this area is hampered by the absence of reliable structural models of column boundaries and by the high computational costs of simulations. Although our SiO_x is amorphous, we distinguish grain boundaries (GBs) and column boundaries (CBs) as interfaces between neighboring oxide columns. When columns are close enough that the atoms at the two sides of the interface can interact, we denote this interface as a grain boundary. On the other hand, where the spacing between the columns is sufficiently large that they do not interact, we call the resultant structure a column boundary. It is illuminating to use experimental findings to construct simple proxies for the SiO_x grain and column boundaries, taking into account that, in most devices, they are exposed to moisture. This allows us to shed light on their role in the mechanisms of resistance changes in columnar films. Previous modeling of the mechanisms of resistance changes in SiO_2 films has focused on the formation of percolation paths in the bulk of amorphous SiO_2[13,20] and at interfaces with electrodes, such as TiN.[21] These calculations have suggested a model, in which electron injection from a cathode into an SiO_2 film facilitates the creation of O vacancies and interstitial O^{2-} ions. The previous calculations demonstrate that O vacancies have low mobility due to high migration barriers,[22] but O^{2-} ions are very mobile in the applied field.[13] In homogeneous films, they diffuse toward a top electrode and can be either trapped at the interface or released into the ambient through grain boundaries in the electrode.[21] Important questions remain regarding the role of GBs and CBs in SiO_x films in the diffusion of O^{2-} ions toward the top electrode and whether CBs trap O^{2-} ions to generate charged interfaces. Furthermore, the interactions of O^{2-} ions with water at grain and column boundaries remain unclear. Addressing these problems may help in understanding the role of GBs and CBs in switching behavior of SiO_2 ReRAM devices.

In this paper, we use high-resolution TEM (HRTEM), electron energy-loss spectroscopy (EELS), energy-dispersive x-ray spectroscopy (EDX), and density functional theory (DFT) modeling to elucidate both the nature of columnar structures in SiO_x and the interaction between metal electrodes and the SiO_x layer. While previously speculated, here, we demonstrate that the space between column edges is best characterized as voids, which facilitate metal incorporation from the Ti and Mo electrodes. Using DFT calculations, we demonstrate that grain and column boundaries fully passivated by silanol groups do not create extra localized electronic states in the bandgap of SiO_2. O^{2-} ions generated in the bulk preferentially migrate to column boundaries where they can react with the silanol groups to form water molecules. These findings provide new insight into the morphology, stability, and evolution of column boundaries, highlighting the pivotal role they play in SiO_x based ReRAM.

II. METHODOLOGY

A. Sample fabrication and preparation

Two ReRAM device heterostructures were studied in this work consisting of Au/Ti–SiO_x–Mo (Au–Ti) and Ti–SiO_x–Mo (Ti) stacks. The base for the Au–Ti device is a Si wafer with 4 μm of thermally oxidized SiO_2 on top, which serves to electrically isolate the ReRAM stack from the Si base wafer. A 210 nm layer of Mo was deposited directly onto the base wafer by magnetron sputtering to form the bottom electrode. A 35 nm layer of SiO_x (x = 1.95) was then deposited on top of the Mo layer using reactive sputtering. For this, an undoped Si target was sputtered in an O/Ar environment where the stoichiometry of the SiO_x film could be controlled by the ratio of O/Ar gas flow. The Au–Ti top electrode was deposited on top of the SiO_x layer by thermal evaporation. A 5 nm Ti layer was first deposited, followed by a 100 nm layer of Au. A shadow mask was used during the top electrode deposition to define individual device sizes. These were selected to be 200 × 200, 400 × 400, 600 × 600, and 800 × 800 μm^2. There was no annealing of the devices as this would promote inter-diffusion and no other post-deposition treatments were applied. The Au–Ti device is optimized for ReRAM performance, containing rough interfaces. In comparison, the Ti device is adapted to allow reliable TEM/EELS measurements to be obtained through relatively smoother interfaces. As such, the fabrication method and stack composition for Ti were similar to those

of Au–Ti. A Si base wafer was used with a 1 μm thermally oxidized SiO_2 layer on top. A 65 nm layer of Mo was then deposited by thermal evaporation giving the bottom electrode. The SiO_x layer was then deposited using the same reactive sputtering method as used in the Au–Ti device, at a thickness of 25 nm. After the SiO_x layer was deposited, a top electrode of Ti (85 nm) was deposited by thermal evaporation. The same shadow mask was used during the top electrode deposition as the Au–Ti device to define the device sizes again ranging from 200 × 200 to 800 × 800 μm^2. Similarly, no annealing or other post-deposition treatments were applied.

B. Structural and elemental characterization (TEM and EELS)

TEM lamellas were prepared using a FEI Helios Nanolab 600 focused ion beam after the deposition of a protective Pt layer. TEM measurements were carried out using a FEI Titan S/TEM microscope. Before measurements, the TEM lamellas were cleaned in an O:Ar plasma for up to 5 min. An acceleration voltage of 200 kV was used with a camera length of 195 mm for all scanning TEM (STEM) high angle annular dark field (HAADF) images and 60 mm for all EELS measurements. EEL spectra were acquired using a Gatan imaging filter (GIF) Tridiem detector with a 2.5 mm aperture, giving a collection semi-angle of 26 mrad with a beam convergence semi-angle of 14 mrad. The acquisition time for EELS measurements was set to values between 50 and 250 ms/pixel. Before each measurement, different acquisition times were tested in a separate region to maximize the EELS signal to noise ratio while ensuring minimal damage to the device. EDX measurements were also taken in the STEM mode, using an EDAX (Model: TOPS 30 OST) EDX detector. For each EDX measurement, the electron beam current was raised by relaxing the gun lens until the EDX counts were ~800–1000 counts/s. Subsequently, a dwell time of 1 ms was used to acquire the EDX spectra using a continuous raster scanning pattern. All data processing was carried out using the Digital Micrograph software. A first degree log polynomial background was used to extract the EELS spectra.[23]

C. Theoretical methodology

DFT calculations were carried out using the Gaussian Plane Wave (GPW) method[24] implemented in the CP2K code.[25,26] The plane wave cut-off and relative cut-off were set to 600 and 60 Ry, respectively, with a convergence criterion of 1×10^{-6} eV per formula unit. Double zeta valence polarized (DZVP) molecularly optimized (MOLOPT) basis sets[27] and Goedecker–Teter–Hutter (GTH) pseudopotentials[28] were used with the Perdew–Burke–Ernzerhof (PBE) functional. The D3-dispersion correction was used to better model the surface interactions, allowing the non-covalent bonds in the system to be more accurately described with the inclusion of long-range electron correlation effects.[29] The SiO_2 grain boundary (GB) and column boundary (CB) models were constructed using a crystalline α-cristobalite (202) surface model. This surface is often used as a mimic for the amorphous SiO_2 surface, more relevant here.[30,31] α-cristobalite and amorphous SiO_2 have very similar bulk densities close to 2.2 g/cm^3. As samples are exposed to an ambient environment during sputter deposition, the boundaries within will have a certain degree of hydroxylation that depends on the device preparation, anneal, and history of operation.[32] Here, we assume that the α-cristobalite surface is fully passivated by silanol Si–O–H groups with a density of 4.72 groups/nm^2, matching closely the surface Si–O–H concentration of a-SiO_2 systems at standard conditions.[32] A 3 × 3 × 5 hydroxylated α-cristobalite (202) surface-slab was used to produce the models where the boundary is formed between the two surfaces of the slab. The lattice parameters were fixed to match those in the bulk of α-cristobalite (468 atoms, a = 1.708 nm, b = 1.491 nm). No translations or rotations were applied between the surfaces. To produce the GB model, a series of CP2K cell optimizations were made to determine the optimal separation between the two α-cristobalite (202) slab surfaces. In each case, the combined system was fully geometry optimized to find the lowest energy configuration for each separation. The lowest energy separation between the two surfaces was used for the grain boundary model (as discussed below).

The O interstitial was considered using a grid-based sampling method to achieve a complete spatial sampling of the system. In this case, a three-dimensional grid with 0.2 nm spacing was generated across a 1 × 1 × 3 unit of the slab. From these, grid points were excluded if an atom within the slab was less than 0.1 nm away. The remaining grid points were used as initial O interstitial site locations, with DFT geometry optimizations carried out for each remaining grid point with an O or O^{2-} interstitial added. The defect formation energy, E_{form}, is calculated using the standard formalism of Zhang and Northrup,[33]

$$E_{form} = E_{Defect} - E_{Bulk} - \sum_i \mu_i n_i + q(\mu_e + E_V),$$

where E_{form} is the defect formation energy, E_{Defect} is the energy of the system with the defect, E_{Bulk} is the energy of the defect free system, μ_i is the chemical potential of the defect species i, n_i is the number species of type i added ($n_i > 0$) or removed ($n_i < 0$) from the system, q is the charge of the system, μ_e is a free parameter representing the electron chemical potential, and E_V is the potential alignment. The chemical potential of O, μ_O, in this work is calculated as one-half the energy of an O_2 molecule in a triplet state.

III. RESULTS

A. HAADF analysis

HAADF STEM images of the Ti [Fig. 1(a)] and Au–Ti [Fig. 1(b)] devices were used to measure the thickness of each layer with the results shown in Table I. Due to the difficulty in resolving the thin Ti layer (~5 nm) in the Au–Ti device, the thickness of the whole top electrode is given. From Fig. 1, it can be found that the Mo layer in each device contains long and thin columns, leading to roughness at the SiO_x/Mo interface. The SiO_x layer is found to have a uniform thickness, which results in the roughness of the SiO_x/Mo interface being conformal to the Me/SiO_x interface.

B. Roughness and patterning

As mentioned earlier, the Mo layer in both devices is comprised of very long and thin columns (Fig. 1). The peaks of the Mo columns form peaks at the Mo/SiO_x interface, while the regions where the columns coalesce form troughs of the Mo/SiO_x interface. The similarity of the Mo layer across both devices is an important observation as it shows that the magnetron sputtering (Au–Ti) and thermal evaporation (Ti) techniques lead to the same microstructure. The low

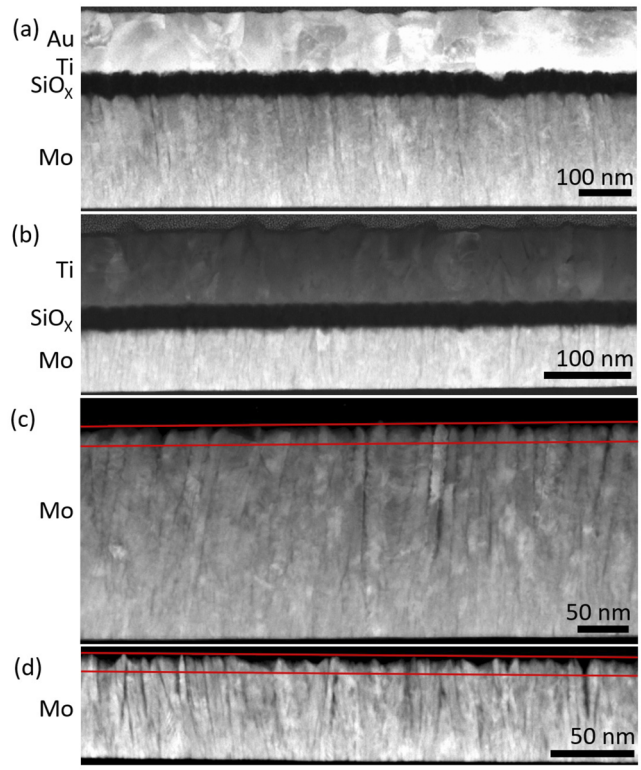

FIG. 1. HAADF image of the (a) Au–Ti device and (b) Ti device. In each case, the Au and Ti top electrodes have a polycrystalline morphology while the Mo layer contains a columnar structure. (c) and (d) HAADF images of the Mo layer in the Au–Ti and Ti devices, respectively. The horizontal red lines mark the minimum and maximum heights of the interface, from which the min/max roughness is estimated to be 11 and 18 nm, respectively.

HAADF intensity regions in between the columns suggest that the column boundaries contain considerably small amounts of material than the column bulk.

The templating of the SiO_x layer by the Mo surface roughness can be seen more clearly in Fig. 2, where SiO_x has a very uniform thickness. This leads to the top surface of the SiO_x layer being highly conformal with the Mo layer. More interestingly, HAADF images [Figs. 2(b) and 2(c)] show how column boundaries propagate from troughs at the SiO_x/Mo interface. The patterning or shadowing effect of the SiO_x column boundaries to the Mo column boundaries can be seen in both the Au–Ti and Ti devices, although the nature of the column boundaries differs quite dramatically for each device. In the Au–Ti device, the column boundaries appear bright in the HAADF images, indicating that they contain more or more dense materials. In this case, the columns can be seen to span the entire SiO_x layer. Conversely, the vast majority of the column boundaries in the Ti device appear with dark contrast, suggesting less or less dense materials. In this case, the width of these boundaries is seen to vary greatly in the device with little correlation to the trough width. Similarly, the height of the boundaries is also variable, with some propagating a few nm into SiO_x and others spanning the entire SiO_x layer. It should be noted that the bright contrast in the Au–Ti device is a result of Mo, Ti, and Au incorporation into the column boundaries during and after fabrication, as discussed below.

TABLE I. The thickness of each constituent layer in the Ti and Au–Ti devices.

	Thickness (nm)	
Layer	Ti	Au–Ti
Top electrode	80	110
SiO_x	25	35
Mo	70	210

C. Columnar boundaries in the Ti device

Figure 2(e) shows the HAADF signal intensity measured along the SiO_x layer in the Ti device. The blue arrows mark four distinct minima and maxima peaks in the intensity, each propagating from trough regions at the SiO_x/Mo interface. The three minima peaks show regions where the HAADF intensity of the SiO_x layer is significantly reduced, dropping to as low as 10% of the mean SiO_x intensity. This suggests that the SiO_x layer contains extremely low-density regions or even voids at the SiO_x/Mo interface trough regions. Although the majority of the column boundaries appear as dark regions, a small number of bright boundaries spanning the SiO_x layer were also observed. In this case, Ti and Mo may have been incorporated into the boundary, as will be discussed below.

D. Column boundaries in the Au–Ti device

Elemental characterization of the Au–Ti device was carried out using EELS and EDX, with the results shown in Fig. 3. Figures 3(a)–3(f) show measurements of the Si $L_{2,3}$ and Si plasmon edges, where the SiO_x column boundary (orange box) and column bulk (blue box) are directly compared. From this, it can be found that both the Si $L_{2,3}$ and Si plasmon edge onset in column boundary and column bulk regions occur at the same energy. Furthermore, the structure of each edge in the boundary and bulk regions is identical. This indicates that the chemical environment of Si is the same, or very similar, in each case. The only difference observed is that the amplitudes of the edges are reduced in the boundary region. The column boundary region in Fig. 3(b) (box dimensions are 5.24 nm width and 22.4 nm height) contains 21% fewer Si $L_{2,3}$ counts. In this case, the counts were measured across an 8 eV width starting from the background-subtracted Si $L_{2,3}$ edge onset at 105 eV. The reduced Si in the boundary region can only be due to an extremely low density SiO_x or, more likely, voids. A 21% reduction in Si counts would correspond to a 1.1 nm void width.

The EDX measurements shown in Figs. 3(g)–3(j) were taken to determine why the column boundary region appeared bright in the STEM images. The red boxes in (g) and (i) mark the regions in the column boundary where the EDX spectra shown on (h) and (j) are collected, respectively. In the region close to the Au–Ti electrode, O, Si, Au, Mo, and Ti are all detected, showing that metal from both electrodes has been incorporated into the boundary. Interestingly, the high Mo count shows that Mo is very mobile in the GB. O, Si, Mo, and Ti were similarly detected in proximity to the Mo electrode, confirming the high mobility of the metal in the columnar

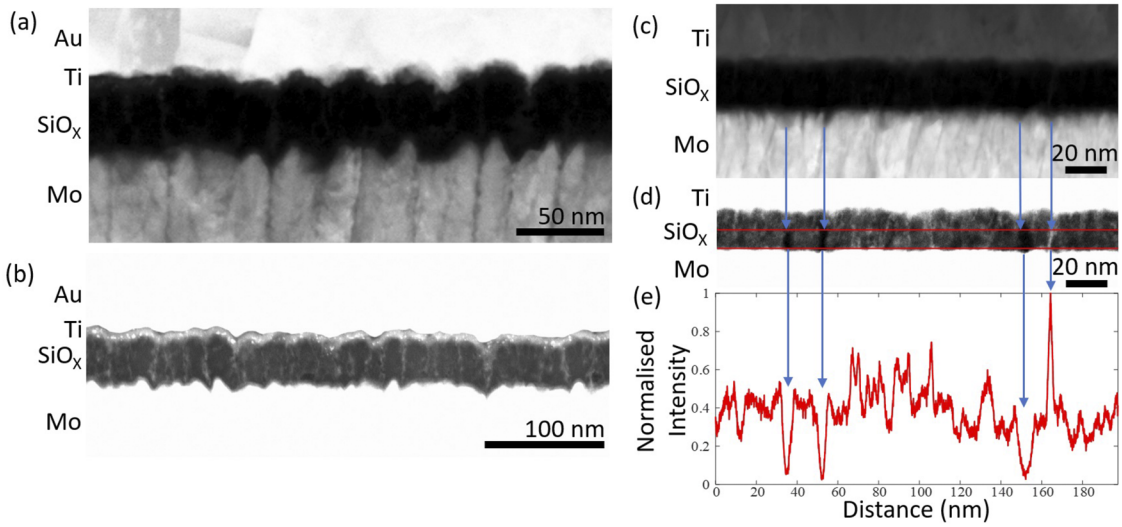

FIG. 2. (a) STEM HAADF cross-sectional image of a pristine Au–Ti device showing the top (Au–Ti) electrode patterns to the Mo electrode roughness. The peaks at the Mo electrode match the peak locations of the Au–Ti electrode. (b) STEM HAADF image of the Au–Ti device. The enhanced brightness highlights the vertical column boundaries protruding from troughs at the SiO_x/Mo interface. (c) HAADF image of the Ti device showing the effect of the SiO_x/Mo interface roughness on the SiO_x microstructure. (d) HAADF image of the Ti device in the same region as (c) with the brightness enhanced to elucidate the SiO_x layer. The horizontal red lines in (d) mark the region in which the normalized HAADF intensity profile (e) is taken. The blue arrows show the position of maxima and minima peaks in the normalized HAADF intensity occurring at trough positions at the SiO_x/Mo interface.

boundaries. The bright contrast can then be understood to result from the surface transport of the metals from the electrodes along the grain boundaries. It should be noted that the Au–Ti device is still in an insulating state, suggesting the formation of metal oxide, which likely plays a role in the resistive switching behavior of the device. We note that the previous study revealed the impact of electrode morphology and the diffusion of Ti from the adhesion layer in the Pt electrode.[34]

E. DFT models of grain and column boundaries

The matching profiles of the Si plasmon and Si $L_{2,3}$ EELS edges show that the chemical environment of Si is the same in the column bulk and boundary regions. The observed significant reduction in Si counts is then best explained as a result of the boundaries containing voids. It is important to note, however, that the exact composition of the surfaces of these column boundaries is unknown as the corresponding EELS signals may be below the resolution limit of the EELS detector. To shed some light on the properties of the void-like boundaries seen above, atomic scale models of SiO_2 grain boundaries (GBs) and column boundaries (CBs) were developed using α-cristobalite as a prototype (see Sec. II C). The two models differ by the separation between the boundary surfaces. The crystalline system was used to decouple the surface and structural disorder effects of amorphous SiO_x, and the α-cristobalite (202) surface was used for its density and the silanol coverage (4.72 per nm^2), which have been shown to be approximately better compared to those of a-SiO_2 systems.[31,32,35]

The lowest energy grain boundary configuration shown in Fig. 4(a) demonstrates the prevalence of inter-surface hydrogen bonds with an O–H bond length of 0.18 nm. In this case, half (2.36 per nm^2) of the silanol groups on each surface participate in inter-surface hydrogen bonds with O from the opposing surface. The remaining silanol groups form in-plane (same surface) hydrogen bonds. A vacuum was then introduced between the two surfaces to model void-like boundaries of widths up to 3.65 nm. The results (Fig. 4) suggest that the two neutral boundary surfaces do not interact at separations >0.65 nm. In this way, we can define GBs as having widths <0.65 nm, where the surfaces are interacting. On the other hand, CBs are the interfaces separated by more than 0.65 nm, where the surfaces are non-interacting. For the remainder of this investigation, the lowest energy configuration with no added separation shown in Fig. 4(a) is used for the GB model and a 2 nm wide void is used for the CB model, where each surface behaves independently [Fig. 4(b)]. By comparing the relative energies of the GB and CB models, the separation energy of two surfaces in the GB model is 3.89 eV/nm^2. The band gaps for the bulk α-cristobalite, GB, and CB models were found to be 6.01, 5.8, and 6.01 eV respectively, suggesting that the surface passivation by silanols leads to only a very small perturbation of the electronic density of states.

Forming and switching of ReRAM devices take place under electron injection conditions. Therefore, the interaction of injected electrons with GBs and CBs considered here is of interest. These effects were considered in Ref. 36, where it has been demonstrated that the two well-known paramagnetic centers of the silica surface, the non-bridging oxygen center and the E' center, are both deep electron traps that are able to form stable, negatively charged surface centers, which can contribute to negative charging of silica surfaces. The formation and concentration of these defects depend on de-hydroxylation reactions at interfaces during device operation, which are considered below. We note that the situation can change significantly if more water is incorporated into CB. However,

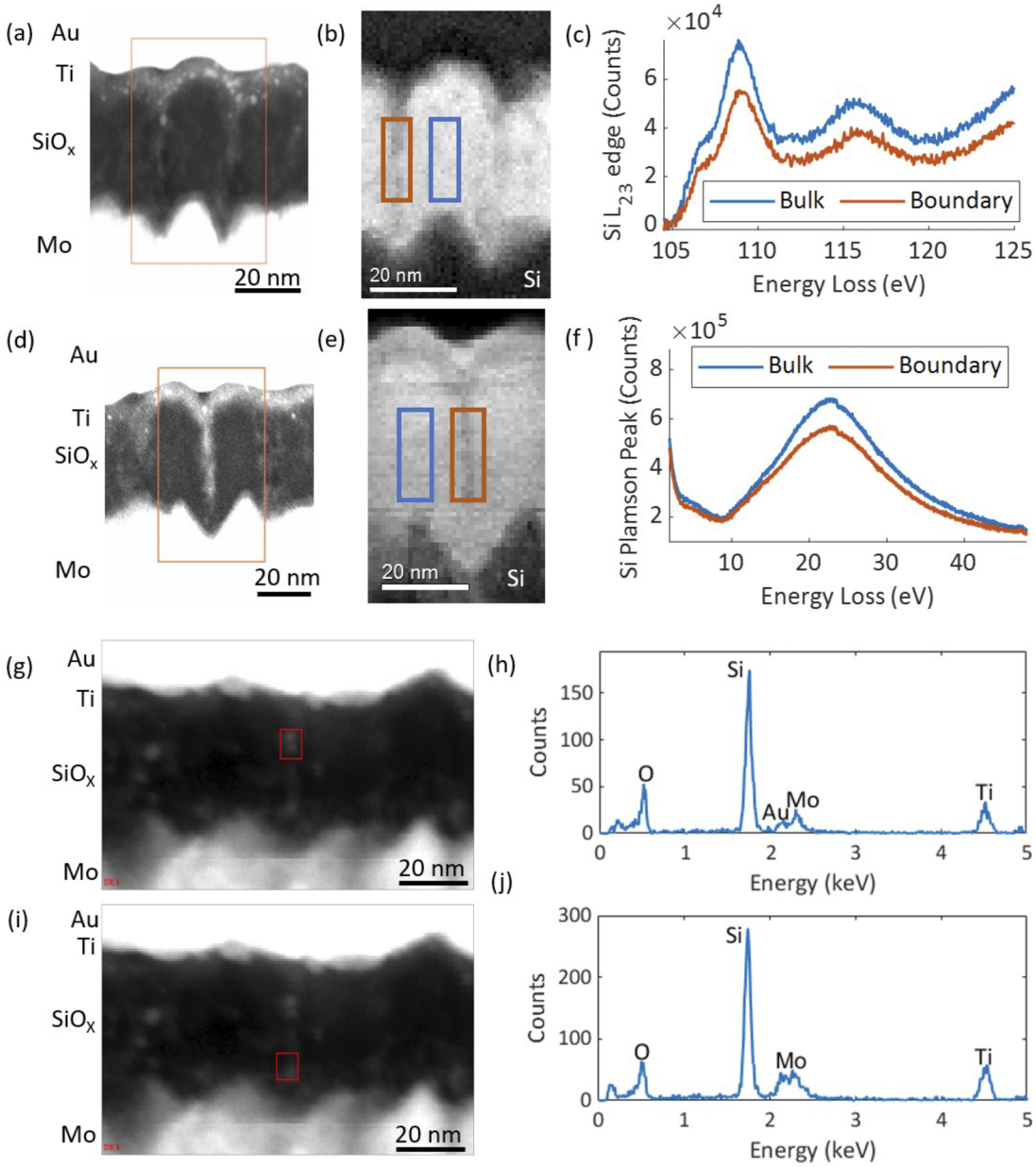

FIG. 3. STEM characterization of the columnar boundaries in the Au–Ti device. (a)–(f) EELS measurements of the Si $L_{2,3}$ and plasmon edges. The orange box on the HAADF images shown in (a) and (d) marks the regions where the (b) Si $L_{2,3}$ and (e) Si plasmon image maps are captured. The orange and blue boxes on (b) and (e) each mark column boundary and column bulk regions, respectively, from which the (c) Si $L_{2,3}$ and (f) Si plasmon spectra are recorded. (g)–(j) EDX measurements taken in the pristine Au–Ti device. The red boxes in (g) and (i) mark the regions in the column boundaries from which the EDX spectra shown in (h) and (j) are collected, respectively.

considering these effects is beyond the scope of this work and warrants a separate study.

F. Reactions of O interstitial defects

According to the dielectric breakdown[37] and electroforming[13,20] models of SiO_2-based devices, O ions are mobile species produced as a result of bias application and electron injection into films. Therefore, we investigate how interstitial O atoms and O^{2-} ions can interact with our model GBs and CBs. O^{2-} ions produced as a result of electron injection[20] will migrate in the field and can discharge near the electrode[21] or as a result of interaction with defects. Therefore, both O atoms and O^{2-} ions are of interest.

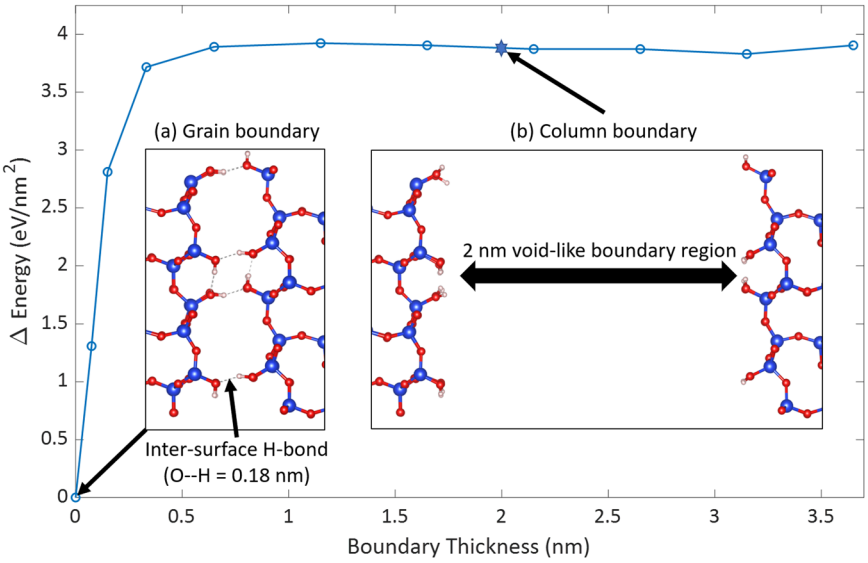

FIG. 4. Surface energy as a function of the column boundary thickness. Insets (a) and (b) show the final α-cristobalite (202) grain boundary and 2 nm column boundary models used in the study. The blue, red, and white spheres correspond to Si, O, and H atoms, respectively.

The distribution of incorporation energies of the neutral O atom into interstitial sites in the GB and CB models was tested using a grid-based sampling method (see Sec. II). In this case, both the bulk α-cristobalite and boundary regions were sampled. The results are summarized in Fig. 5(a), where the y axis is given as a function of distance (Z) from the GB and CB surfaces into the bulk, where Z = 0 at the surface of the boundary. Negative Z values represent O incorporation toward the α-cristobalite bulk. In the bulk, the lowest energy and most stable defect was the O interstitial, where the incorporation energy was found to vary between 1.5 and 2 eV across all O interstitial sites. In the GB and CB boundaries, however, the O interstitial was found to be a high energy defect with incorporation energies between 3 and 3.5 eV [Fig. 5(d)]. Instead, a hydrogen passivated O peroxy radical defect is favored, with the O incorporation energy reducing to below 1 eV at some sites. Figures 5(b) and 5(c) show the two configurations of O peroxy-type defects we observed. In GB models, the hydrogen passivated O peroxy radical may form a hydrogen bond with the opposite surface, as shown in Fig. 5(b). In CB models, the peroxy defect forms hydrogen bonds with O at the same surface. It should be noted that, in both cases, the H atom of the peroxy bridge also forms a H bond with an O atom in the bridge [Figs. 5(b) and 5(c) (inset)]. With a large number of sites found that have incorporation energies lower than bulk α-cristobalite, it is expected that O will preferentially reside in the boundaries, most likely in the form of peroxy-type defects.

Figure 6(a) shows the incorporation energy of the O^{2-} ion into the GB and CB models (Z = 0 at the column boundary surface). The mean incorporation energy of the O^{2-} ion across all bulk sites is used to center the data for direct comparison. The results show that the

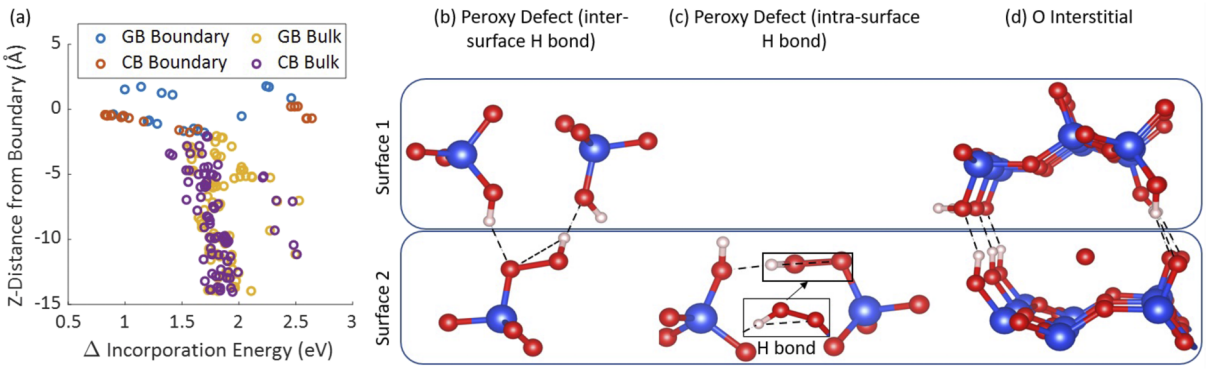

FIG. 5. (a) The incorporation energy of O in the α-cristobalite grain and column boundaries. Z = 0 represents the surface of the boundaries and negative Z values represent O incorporation toward the α-cristobalite bulk. (b)–(d) Schematic of the O defects found in the GB and CB models. The blue, red, and white spheres correspond to Si, O, and H atoms, respectively. (b) Peroxy defect found in the GB model, which forms hydrogen bonds to the opposing surface. (c) Peroxy defect found in both the GB and CB models, which forms hydrogen bonds to the same surface. (d) O interstitial defect in a GB model (high energy defect).

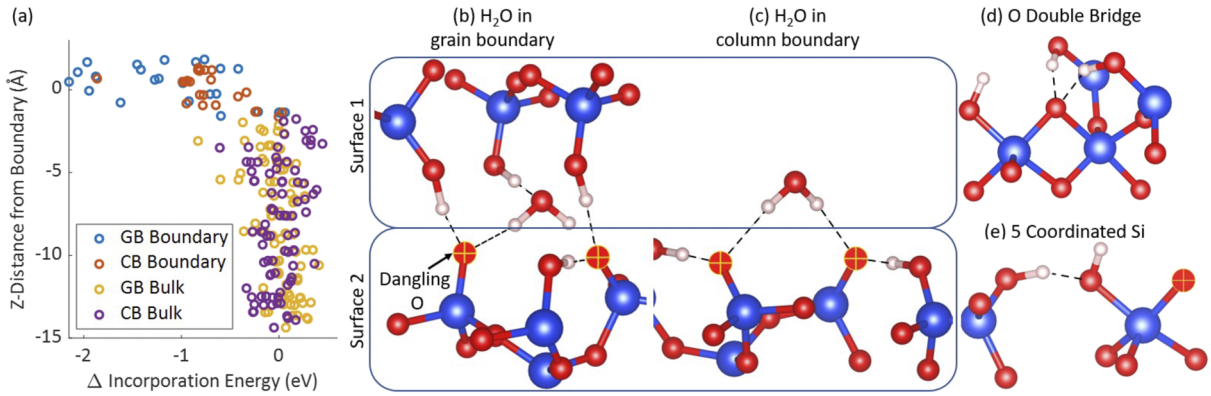

FIG. 6. (a) The incorporation energy of the O^{2-} ion in the α-cristobalite grain and column boundaries. Z = 0 represents the surface of the boundaries and negative Z values represent O^{2-} incorporation toward the α-cristobalite bulk. (b)–(e) Schematic of the O^{2-} defects found in the GB and CB models. The blue, red, and white spheres correspond to Si, O, and H atoms, respectively. (b) and (c) show the formation of water molecules along dangling O in the GB and CB models, respectively. In this case, dangling O atoms are marked as red spheres containing a yellow cross. (d) and (e) show the O double bridge and five coordinated Si defects, respectively, which are both high energy defects.

GB and CB models behave differently, with O^{2-} more favored to reside in the GB. This was found to be due to the additional surface providing more silanol groups for hydrogen bonding. Across the 24 O^{2-} sites sampled in the GB, all sites were lower in energy than the mean bulk incorporation energy. Furthermore, 12 of 24 sites gave an incorporation energy of >1 eV lower than the mean bulk energy. In 10 of these sites, O^{2-} was found to scavenge hydrogen from surface silanol groups to form water molecules to leave dangling O, as shown in Fig. 6(b). In each case, the GB structure relaxed to maximize hydrogen bonding between the two surfaces of the GB, the water molecule, and the dangling O, where water and the dangling O each formed two hydrogen bonds. This suggests that O^{2-} ions will have a strong thermodynamic drive to migrate into the GB and remain as water.

Only one low energy water configuration was found in the CB (1.9 eV lower than the mean bulk O^{2-} incorporation energy), as shown in Fig. 6(c). From this, it can be found that hydrogen bond formation is favored in a similar fashion to the case of the GB. Of the remaining 14 water sites, fewer hydrogen bonds formed leaving either water or a dangling O to form one hydrogen bond. The incorporation energy of these sites was found to be between 0.5 and 1 eV lower than the mean incorporation energy.

Furthermore, OH^- hydroxyl groups were found to form in both the GB and CB models, suggesting that the formation of water may occur in the two-step process,

$$O^{2-} + H^+ \rightarrow OH^-,$$

$$OH^- + H^+ \rightarrow H_2O.$$

Two high energy defect configurations identified in both the GB and CB were the O double bridge [Fig. 6(d)] and the five coordinated Si [Fig. 6(e)]. In the O double bridge configuration, the incorporated O forms a siloxane linkage to an existing Si–O–Si bond to form an O double bridge. In the five coordinated Si configuration, the incorporated O bonds to a surface Si atom, resulting in a dangling O that traps Mulliken charge between 0.5 and 0.7$|e|$.

These results demonstrate that both neutral and charged oxygen atoms prefer to move to GBs and CBs and reside there, forming peroxy species and water molecules. From this perspective, these GB and CB models do not serve as highways for oxygen diffusion toward a top electrode in devices. Initial migration of O^{2-} ions to boundaries will lead to their charging and reduce their ability to trap oxygen. The direction of CBs along the field and the formation of water molecules reduce the ability of oxygen ions trapped at CBs to participate in set/reset processes by moving in/out of these interfaces. However, further study is required to determine the effects of mass O and O^{2-} incorporation in the boundaries.

IV. DISCUSSION AND SUMMARY

The STEM images of the Au–Ti and Ti devices obtained in this work show that the roughness of the Mo layer templates the SiO_x layer sputtered on the top. In each device, columnar boundaries are seen to protrude into the SiO_x layer, located at troughs of the SiO_x/Mo interface. However, the nature of the column boundary turns out to be markedly different between the devices. In the Ti device, STEM images show that the majority of the column boundary regions give dark contrast, with the STEM intensity reducing to as low as 10% of the mean SiO_x intensity. Such a reduction in intensity suggests that these boundaries are void-like. The STEM images also show that the width and height of these void-like boundaries vary with no significant correlation to the dimensions of the trough. In a very small number of cases, bright columnar boundaries were seen, which are the result of metal incorporation into the column boundary.

In the Au–Ti device, however, all column boundaries are bright in contrast. In this case, the boundaries span from the SiO_x/Mo interface across the SiO_x layer to the Au–Ti/SiO_x interface. The intensity of the Si plasmon and $L_{2,3}$ edges at boundaries compared to the boundary bulk show that there is a reduction in Si counts (21% for the Si $L_{2,3}$ counts). Furthermore, the edges at the boundary and bulk regions are almost identical, suggesting that Si is in a similar chemical environment in each region. This is further evidence

that these regions are void-like. Instead, the bright intensity of these regions is due to Mo and Ti incorporation into the boundary. The devices are each in an insulating state, which suggests that the metal that has incorporated is in a high oxidation state. We speculate that the difference in the characteristics of the column boundary between the two devices is due to two reasons. First, the SiO_x/Mo interface is considerably rougher in the Au–Ti device, which is expected to result in a different column boundary morphology. Second, the effect of O exchange may play an important role in the characteristics of the boundaries. In both devices, Ti, Si, and Mo are each competing for O. With only a 5 nm layer of Ti in the Au–Ti device, less Ti is available to incorporate into the device. As a result, there is less competition for the formation of MoO_x at the SiO_x/Mo boundary in the Au–Ti device, in turn facilitating the incorporation of Mo into the boundary.

To better understand the chemistry of the column boundaries, DFT models were created using hydroxylated α-cristobalite (202) surfaces. The results show that the grain boundary is the most stable configuration, giving lowest energy due to maximizing the number of inter-surface hydrogen bonds (length = 0.18 nm). It was then shown that the two surfaces do not interact at separations > 0.65 nm, with a separation energy of 3.89 eV/nm^2. The gaps between column boundaries observed in the Ti and Au–Ti devices are larger than 0.65 nm, suggesting that the surfaces of the column boundaries in the studied devices are independent.

The results of DFT calculations show the propensity of O and O^{2-} interstitial defects to move and get trapped at GBs and CBs. Neutral O atoms form peroxy defects on the surface, with the O interstitial being a high energy defect. In the −2 charge state, O was found to favor water formation, leaving dangling O bonds on the boundary surfaces. In this case, more and lower energy sites were found in the GB model due to the increased surface silanol availability for the water and dangling O bonds to form hydrogen bonds. The direction of CBs along the field could facilitate the migration of O ions toward the electrodes. However, the formation of water molecules reduces the ability of oxygen ions trapped at CBs to escape and to participate in set/reset processes by moving in/out of these interfaces.

To summarize, our experimental results elucidate details of the complex morphology of the columnar microstructure of SiO_x films and metal electrodes used in successful ReRAM devices and suggest that the space between most of the column boundaries in SiO_x films is void. Furthermore, EELS and EDX characterization techniques show that both Ti and Mo from the electrodes can diffuse along the oxide column boundaries, adding significant complexity to the mechanism of resistance switching. Atomistic modeling of the oxygen ion behavior at column boundaries demonstrates that they are immobilized inside the column boundary and as such not available to take an active part in set and reset processes.

ACKNOWLEDGMENTS

K.P. acknowledges the A*STAR Graduate Academy for its graduate scholarship under the ARAP program. The authors also acknowledge funding provided by EPSRC (Grant No. EP/L015862/1) and the use of the ARCHER High Performance Computing Facility via membership to the UK's HPC Materials Chemistry Consortium, which is funded by EPSRC (Grant No. EP/L000202). J.C., A.J.K., and A.L.S. acknowledge the Leverhulme Trust for funding part of this work (Grant No. RPG-2016-135), and M.B. acknowledges support from the Ministry of Education (MOE) Singapore, under AcRF Tier 1 startup Grant No. R-284-000-179-133. A.M. acknowledges the Royal Academy of Engineering and the support through the research fellowship.

AUTHOR DECLARATIONS

Conflict of Interest

■.

DATA AVAILABILITY

The data that support the findings of this study are available from the corresponding author upon reasonable request.

REFERENCES

[1] R. Waser and M. Aono, Nat. Mater. **6**, 833 (2007).
[2] M. A. Zidan, J. P. Strachan, and W. D. Lu, Nat. Electron. **1**, 22 (2018).
[3] M. Lanza, H.-S. P. Wong, E. Pop, D. Ielmini, D. Strukov, B. C. Regan, L. Larcher, M. A. Villena, J. J. Yang, L. Goux, A. Belmonte, Y. Yang, F. M. Puglisi, J. Kang, B. Magyari-Köpe, E. Yalon, A. Kenyon, M. Buckwell, A. Mehonic, A. Shluger, H. Li, T.-H. Hou, B. Hudec, D. Akinwande, R. Ge, S. Ambrogio, J. B. Roldan, E. Miranda, J. Suñe, K. L. Pey, X. Wu, N. Raghavan, E. Wu, W. D. Lu, G. Navarro, W. Zhang, H. Wu, R. Li, A. Holleitner, U. Wurstbauer, M. C. Lemme, M. Liu, S. Long, Q. Liu, H. Lv, A. Padovani, P. Pavan, I. Valov, X. Jing, T. Han, K. Zhu, S. Chen, F. Hui, and Y. Shi, Adv. Electron. Mater. **5**, 1800143 (2019).
[4] D. Ielmini, Semicond. Sci. Technol. **31**, 063002 (2016).
[5] X. Hong, D. J. Loy, P. A. Dananjaya, F. Tan, C. Ng, and W. Lew, J. Mater. Sci. **53**, 8720–8746 (2018).
[6] A. Mehonic, A. Sebastian, B. Rajendran, O. Simeone, E. Vasilaki, and A. J. Kenyon, Adv. Intell. Syst. **2**, 2000085 (2020).
[7] R. Waser, R. Dittmann, G. Staikov, and K. Szot, Adv. Mater. **21**, 2632–2663 (2009).
[8] C. Wang, H. Wu, B. Gao, T. Zhang, Y. Yang, and H. Qian, Microelectron. Eng. **187-188**, 121 (2018).
[9] H.-S. P. Wong, H.-Y. Lee, S. Yu, Y.-S. Chen, Y. Wu, P.-S. Chen, B. Lee, F. T. Chen, and M.-J. Tsai, Proc. IEEE **100**, 1951 (2012).
[10] A. Mehonic, M. S. Munde, W. H. Ng, M. Buckwell, L. Montesi, M. Bosman, A. L. Shluger, and A. J. Kenyon, Microelectron. Eng. **178**, 98 (2017).
[11] A. Mehonic, A. L. Shluger, D. Gao, I. Valov, E. Miranda, D. Ielmini, A. Bricalli, E. Ambrosi, C. Li, J. J. Yang, Q. Xia, and A. J. Kenyon, Adv. Mater. **30**, 1801187 (2018).
[12] K.-C. Chang, T.-M. Tsai, T.-C. Chang, H.-H. Wu, J.-H. Chen, Y.-E. Syu, G.-W. Chang, T.-J. Chu, G.-R. Liu, Y.-T. Su, M.-C. Chen, J.-H. Pan, J.-Y. Chen, C.-W. Tung, H.-C. Huang, Y.-H. Tai, D.-S. Gan, and S. M. Sze, IEEE Electron Device Lett. **34**, 399 (2013).
[13] A. Mehonic, M. Buckwell, L. Montesi, M. S. Munde, D. Gao, S. Hudziak, R. J. Chater, S. Fearn, D. McPhail, M. Bosman, A. L. Shluger, and A. J. Kenyon, Adv. Mater. **28**, 7549 (2016).
[14] A. Mehonic and A. J. Kenyon, in *Defects at Oxide Surfaces*, edited by J. Jupille and G. Thornton (Springer International Publishing, Basel, Switzerland, 2015), pp. 401–428.
[15] M. S. Munde, A. Mehonic, W. H. Ng, M. Buckwell, L. Montesi, M. Bosman, A. L. Shluger, and A. J. Kenyon, Sci. Rep. **7**, 9274 (2017).
[16] W. Jung, J. O. Dereux, W. C. Chueh, Y. Hao, and S. M. Haile, Energy Environ. Sci. **5**, 8682 (2012).
[17] Y. Zhang, Y. Liu, and M. Liu, Chem. Mater. **18**, 4643 (2006).
[18] H.-C. Chen, C.-C. Lee, C.-C. Jaing, M.-H. Shiao, C.-J. Lu, and F.-S. Shieu, Appl. Opt. **45**, 1979 (2006).

[19]C. L. Jia, K. Urban, S. Hoffmann, and R. Waser, J. Mater. Res. **13**, 2206 (1997).
[20]D. Z. Gao, A.-M. El-Sayed, and A. L. Shluger, Nanotechnology **27**, 505207 (2016).
[21]J. Cottom, A. Bochkarev, E. Olsson, K. Patel, M. Munde, J. Spitaler, M. N. Popov, M. Bosman, and A. L. Shluger, ACS Appl. Mater. Interfaces **11**, 36232 (2019).
[22]M. S. Munde, D. Z. Gao, and A. L. Shluger, J. Phys.: Condens. Matter **29**, 245701 (2017).
[23]R. F. Egerton, "Quantitative analysis of energy-loss data," in *Electron Energy-Loss Spectroscopy in the Electron Microscope* (Springer, Boston, MA, 2011), pp. 231–291.
[24]G. Lippert, J. Hutter, and M. Parrinello, Mol. Phys. **92**, 477 (1997).
[25]J. VandeVondele, M. Krack, F. Mohamed, M. Parrinello, T. Chassaing, and J. Hutter, Comput. Phys. Commun. **167**, 103 (2005).
[26]J. Hutter, M. Iannuzzi, F. Schiffmann, and J. Vandevondele, Wiley Interdiscip. Rev.: Comput. Mol. Sci. **4**, 15 (2014).
[27]J. VandeVondele and J. Hutter, J. Chem. Phys. **127**, 114105 (2007).
[28]S. Goedecker, M. Teter, and J. Hutter, Phys. Rev. B **54**, 1703 (1996).
[29]S. Grimme, J. Antony, S. Ehrlich, and H. Krieg, J. Chem. Phys. **132**, 154104 (2010).
[30]A. Rimola, D. Costa, M. Sodupe, J.-F. Lambert, and P. Ugliengo, Chem. Rev. **113**, 4216 (2013).
[31]F. S. Emami, V. Puddu, R. J. Berry, V. Varshney, S. V. Patwardhan, C. C. Perry, and H. Heinz, Chem. Mater. **26**, 2647 (2014).
[32]L. T. Zhuravlev, Colloids Surf., A **173**, 1 (2000).
[33]S. B. Zhang and J. E. Northrup, Phys. Rev. Lett. **67**, 2339 (1991).
[34]J. J. Yang, J. P. Strachan, Q. Xia, D. A. A. Ohlberg, P. J. Kuekes, R. D. Kelley, W. F. Stickle, D. R. Stewart, G. Medeiros-Ribeiro, and R. S. Williams, Adv. Mater. **22**, 4034 (2010).
[35]F. Federici Canova, M. Mizukami, T. Imamura, K. Kurihara, and A. L. Shluger, Phys. Chem. Chem. Phys. **17**, 17661 (2015).
[36]L. Giordano, P. V. Sushko, G. Pacchioni, and A. L. Shluger, Phys. Rev. Lett. **99**, 136801 (2007).
[37]A. Padovani, D. Z. Gao, A. L. Shluger, and L. Larcher, J. Appl. Phys. **121**, 155101 (2017).